



Ceramics based on concrete wastes prepared by spark plasma sintering

Mohammed Abass¹, Yasuyuki Kanda^{2,*}

¹*Mechanical Systems Engineering Course, Graduate School of Engineering and Science, University of the Ryukyus, 1 Senbaru, Nishihara-Cho, Nakagami-gun, Okinawa 903-0213, Japan*

²*Mechanical Engineering Program, School of Engineering, University of the Ryukyus 1 Senbaru, Nishihara-Cho, Nakagami-gun, Okinawa 903-0213, Japan*

Received 28 September 2020; Received in revised form 5 January 2021; Accepted 3 March 2021

Abstract

An effective utilization technique is required to recycle fine aggregate in concrete waste because the presence of residual waste cement reduces the quality of the recycled concrete. In this study, recycled aggregate powder (RAP) was prepared by milling Okinawan concrete waste and developing a ceramic compact with high flexural strength using the spark plasma sintering (SPS) method. The RAP raw material consisted mainly of calcite and quartz. The densification gradient of the sintered compact was uniform during sintering at 1123–1273 K. At 1273 K sintering temperature, Vickers hardness (HV) obtained a maximum of 393 along with 78.9 MPa maximum flexural strength, which exceeded the porcelain stoneware tile ISO 13006 standards. Scanning electron microscopy with energy dispersive X-ray (SEM-EDX) element analysis suggested that the inner structure constituted unmelted silica-rich sand particles and melted calcium-rich particles containing waste cement and fine aggregate with limestone. Therefore, it can be concluded that SPS progressed by the liquid-phase sintering phenomenon between sand particles and calcium-rich particles, which contributed to flexural strength and modulus improvement.

Keywords: concrete waste, recycled fine aggregate, spark plasma sintering, mechanical properties

I. Introduction

Concrete is widely used in the construction and infrastructure industries owing to its excellent mechanical properties and durability. Infrastructural modification and house building activities result in a large amount of constructional and demolition waste. Billions of tons of concrete waste are produced worldwide every year as industrial by-products of construction and demolition [1–3].

Currently, a certain quantity of concrete waste is recycled as landfill, used in road construction as an unbound road sub-base or roadbed material, and reused with fresh concrete to produce recycled concrete aggregate [4–16]. However, roadbed material demands are expected to reduce. Additionally, recycled concrete produces low-quality concrete due to residual waste cement [11]. Thus, effective concrete waste recycling is desirable for environmental protection and to prolong the usable life of worldwide final disposal sites. A method to

form recycled fine aggregate, which mainly constitutes mortar, must be developed as the removal of waste cement by milling or peeling is difficult.

In the ceramics processing field, industrial wastes such as fly ash were effectively utilized as the raw material for ceramics [17–20]. Fly ash has very fine particles with an average diameter of approximately 10 μm , and it is chemically made of SiO_2 and Al_2O_3 . Similarly, municipal solid waste ash [21,22], blast furnace slag [23–26], sewage sludge [27,28], and bagasse ash [29–31] have been suggested as raw material for ceramic processing. Furthermore, it has been suggested that materials with superior mechanical strength can be developed using the spark plasma sintering (SPS) method with industrial waste as a ceramic raw material [31–35]. The SPS method, which sinters raw material powders within a graphite mould under compression pressure, lowers the sintering temperature and produces materials with superior mechanical properties as compared to hot pressing [36–40]. Thus, a material with superior density can be made in a shorter sintering time as compared to that made using ordinary electric furnace sintering. In-

*Corresponding author: tel: +81 988958631, e-mail: kanda@tec.u-ryukyu.ac.jp

dustrial waste material such as fly ash can be used as a structural material based on previous studies demonstrating ceramic SPS [32–34]. In the SPS process for fly ash and clay composite material, the improvement in flexural strength was revealed by liquid-phase sintering between unmelted fly ash and melted clay [32]. Elsie *et al.* [39] investigated the fabrication of mullite from lithomargic clay using the SPS method without the addition of binders. Recycled fine aggregate mainly constitutes the mortar part; its chemical composition includes SiO_2 , Al_2O_3 , and CaO , in the form of fly ash or clay [41]. The development of glass-ceramics using concrete sludge has been reported in the literature [42–45]. Thus, recycled aggregate powder (RAP), which is produced by milling recycled fine aggregate, may be used as a raw material for ceramics. In addition, the development of ceramics with superior mechanical properties can be expected upon applying the SPS method.

This study investigates the SPS process using RAP as a novel recycling method for concrete waste for application in ceramics processing. According to the ISO 13006 standards, ceramic tiles having strength greater than 35 MPa are better suited for porcelain stoneware tiles [30,46]. We apply the SPS technique for sintering RAP to produce ceramics that have a flexural strength greater than 70 MPa, which is double the value set by the ISO 13006 standards. The key to ceramic sintering is the optimum sintering temperature for raw materials. Therefore, the optimum SPS sintering temperature for RAP was investigated to improve the mechanical properties of the ceramic compact. The ceramic compact was validated by evaluating its mechanical properties as compared to the characteristics of ordinary concrete and sintered fly ash compact using SPS. Finally, we discuss the behaviour of RAP during the SPS processing by analysing the surface structure of the sintered compacts using scanning electron microscopy-energy dispersive X-ray spectroscopy (SEM-EDX), thermogravimetric-differential thermal analysis (TG-DTA) of the RAP and the relationship between the displacement and sintering temperature in the SPS process.

II. Experimental

2.1. Materials

Recycled aggregate powder (RAP), which is the experimental raw material, was prepared by crushing, sieving and wet pot milling of concrete waste [47]. We used the concrete waste YUIKURU (RC-40), which is certified and authorized by the Okinawa prefecture government in Japan. This concrete waste with a fine aggregate composition consists of sea sand, limestone and the shells of sea creatures. Thus, the chemical composition of the used concrete waste is expected to be calcium-rich as compared to that of typical concrete. The concrete waste was crushed into 10 mm length cubes using a Joe Crusher (Yoshida Manufacturing Co. Ltd, 1023B). The crushed concrete waste was sieved using an open

sieve of mesh size 425 μm and then milled using a pot mill apparatus (AS ONE Corporation, PM-001). For pot milling preparation, 300 g of prepared concrete waste, $10 \times \varnothing 30$ mm, $15 \times \varnothing 25$ mm alumina balls and 300 g of ion-exchange water were added to a 1 l alumina pot. Pot milling was performed at 200 rpm for 12 h. After milling, the RAP slurry was dried for 2 h at 393 K. We measured the particle size distribution of RAP using a particle size analyser (MicrotracBEL Corp., MT3300). The average particle size was 9.4 μm [47].

2.2. Spark plasma sintering (SPS)

The RAP was sintered using an SPS apparatus (Sumitomo Coal Mining Co., Ltd., Dr. Sinter SPS-2050). The RAP raw material was poured into a graphite mould capped by pairing two punches ($\varnothing 50$ mm) and die (inner $\varnothing 50$ mm, outer $\varnothing 90$ mm). The graphite mould was covered with carbon felt to prevent heat from radiating out during the sintering process. A 20 MPa pressure, 20 min sintering time, and 1123–1273 K sintering temperatures were set as the SPS sintering conditions. The heating rates were 42.5–50 K/min. The holding time for each sintering temperature was 5 min. The current was turned off as the holding time elapsed and the cooling rate was furnace cooling. These SPS conditions were referred to from literature based on SPS [31,32]. Subsequently, the samples were removed from the graphite mould. The SPS sintered compact was 5 mm thick with a diameter of 50 mm.

2.3. Characterization

A three-point bending test was performed on specimens obtained by cutting the sintered compacts into bars. These bars were 7 mm in width, 40 mm in length, and 3 mm in height. We attached the strain gauge (Kyowa Electronic Instruments Co., Ltd., KFGS-1-120-C1-11L1M2R) at the bottom centre of the specimen. Three specimens were used for each SPS condition. The three-point bending test was performed with a 0.5 mm/min crosshead speed and a 40 mm support span. In addition, the stress-strain curve was recorded using a digital oscilloscope (Yokogawa Electric Co., Ltd., DL 750P). The flexural strength, σ_f was calculated using following equation:

$$\sigma_f = \frac{3F \cdot L}{2b \cdot h^2} \quad (1)$$

where F is the maximum load, L is the support span, b is the specimen width, and h is the specimen height. Furthermore, the flexural modulus, which is the slope of the stress-strain curve in the elastic region, was calculated using the least square method.

The Vickers hardness test was performed on the specimen surface after the three-point bending test using an Akashi Co. Ltd. (MVK-G1) with a load and loading time of 500 g and 15 s, respectively. To investigate the densification gradient, the specimen was divided into five parts from the specimen centre. The measurement was conducted at 10 points for each division point, as

shown below. To avoid indentation load influence on flexural strength and modulus, we used the HV specimen after the three-point bending test. However, work hardening did not occur in the HV specimen due to the sintered compact being ceramics. Thus, the HV values are not affected by the three-point bending test.

The surface structure and elemental composition of the sintered compacts were observed and analysed using SEM-EDX (Hitachi High-Technologies, TM3030).

RAP thermal analysis was performed using a TG-DTA apparatus (RIGAKU Corp., Thermo plus EVO2 TG-DTA/H-S) up to 1623 K temperature and 20 K/min heating rate under air and N₂ environments.

X-ray fluorescence analysis was performed on Shimadzu Corporation, EDX-8000.

III. Results and discussion

Table 1 shows chemical composition of RAP determined using energy dispersive X-ray fluorescence analysis [47]. The RAP chemical components constituted mainly CaO and SiO₂ with small amount of Al₂O₃ and Fe₂O₃. The chemical composition of RAP resembles fly ash or clay [32–35,42–44]. Percentage of CaO was higher than that in the concrete waste [41] owing to the waste concrete features mentioned earlier. To further investigate the fundamental characteristics of RAP, we conducted powder X-ray diffraction (XRD). Figure 1 shows the XRD pattern of RAP. The peak showed the presence of calcite (CaCO₃) and quartz (SiO₂). This analysis is similar to that of recycled fine aggregate based on the existing literature [12]. Thus, the chemical composition of CaO is mainly calcite, which is derived from waste cement and fine aggregate of the Okinawan concrete.

Table 1. Chemical composition of RAP in wt.% [47]

CaO	SiO ₂	Al ₂ O ₃	Fe ₂ O ₃	SO ₃	MgO	other
57.3	27.5	5.86	4.16	2.24	1.21	1.73

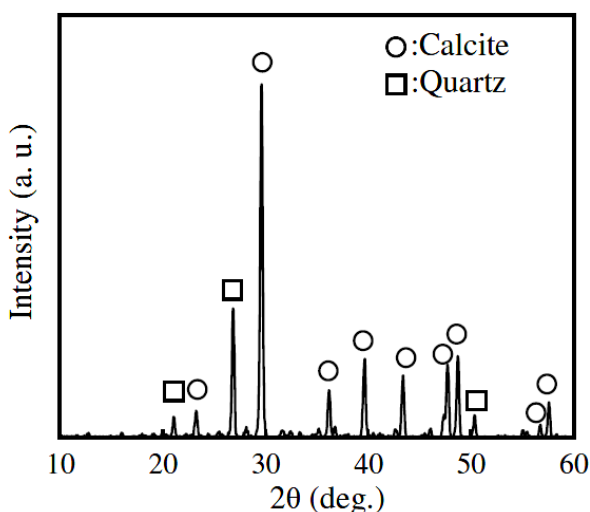


Figure 1. X-ray diffraction pattern of RAP

Figure 2 shows the relationship between relative density and sintering temperature. The theoretical density was calculated using the chemical components in Table 1 and Fig. 1. Thus, CaO is substituted with CaCO₃ and gives a theoretical density value of 2.8 g/cm³. Moreover, the density of the SPS sintered compacts was measured by dividing the weight of sample by its volume. The relative density linearly increased to almost 1.0 as the temperature reached 1223 K. Increasing the sintering temperature to 1273 K resulted in a decrease in relative density. Melted RAP was observed around the graphite punch after raising the temperature to 1273 K. This indicated that melting occurred during sintering at over 1223 K due to the generation of micro inner pores at temperatures close to 1273 K. The maximal density of the SPS sintered compact, 2.8 g/cm³, is higher than that of typical concrete 2.4 g/cm³. The concrete curing procedure is a hydration reaction between cement and water without the application of compression pressure during curing. It is well known that approximately 3% of the inner structure of concrete contains pores. The SPS sintered compact utilized the sintering phenomenon as a curing procedure; during sintering, the applied compression pressure assisted the escape of gases trapped in the raw powders. Thus, the SPS sintered compacts were denser than typical concrete. As a preliminary experiment, we conducted the SPS experiment for applied pressures over 20 MPa. As a result, the mechanical properties reduced at 30 MPa, and the graphite mould broke at 40 MPa. For future work, we will consider utilizing a high-strength mold to apply a 40 MPa pressure.

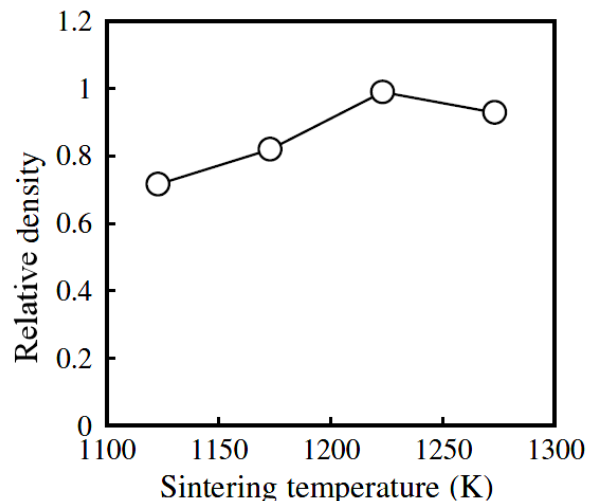
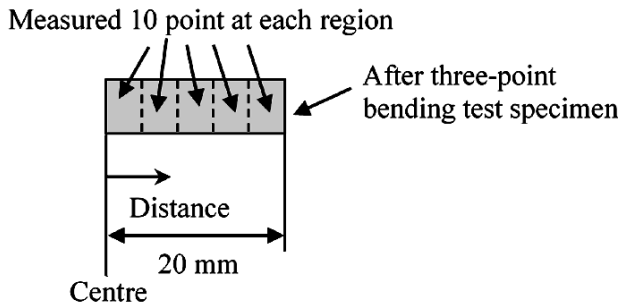


Figure 2. Relationship between relative density and sintering temperature

To investigate the densification gradient and performance of the mechanical properties, a Vickers hardness test was conducted. Figure 3 shows the relationship between HV and the distance from the centre in the three-point bending test specimen. In this test, the distance was measured using the average length at each point (2.0, 6.0, 10.0, 14.0 and 18.0 mm). The HV distribution within the SPS sintered sample was almost uniform for



Schematic diagram of measurement

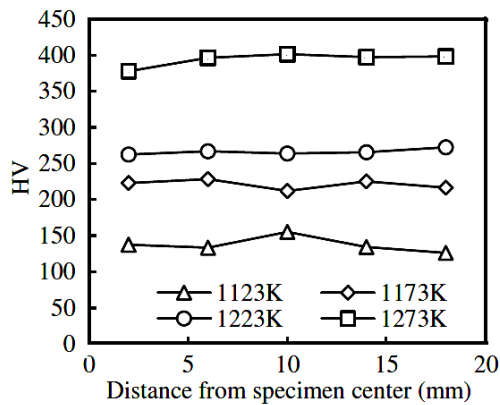


Figure 3. Relationship between HV and distance from specimen centre in three-point bending test specimen

each sintering temperature. Thus, the density gradient was not recognized in the sintered compact. The average HV of the five points increased with increasing sintering temperature, and the maximum value obtained was 393 at a sintering temperature of 1273 K. The concrete HV is approximately 100, based on the literature [48]. The SPS sintered sample's HV is higher than that of concrete due to the curing process difference between the concrete and SPS methods, as mentioned in the discussion of relative density. The HV of the SPS sintered compact is lower than that of SPS sintered fly ash HV, which is approximately 850 [32]. The HV of lime ceramics is approximately 190–260 [49], commercial window glass is 420 [44] and alumina (Al_2O_3) ceramics sintered by SPS is approximately 2000 [50]. SiO_2 and Al_2O_3 content in fly ash are higher than those in RAP [32]. Thus, we inferred that the SPS sintered compact's HV was lower than that of the fly ash SPS compacts. Compared to the HV of other materials, general steel and aluminium (Al) alloy powders sintered by SPS have approximately 200–300 [33] and 84 [51], respectively. Therefore, the HV of the SPS sintered compact is superior to that of other structural materials.

The effects of current flow during the SPS process on the temperature distribution of the compressed RAP in a graphite mould are also important. The electrical resistances of individual components of RAP were as follows: CaCO_3 $6.7 \times 10^4 \Omega\cdot\text{m}$ [52], $\text{SiO}_2 > 10^{12} \Omega\cdot\text{m}$ on

SiO_2 glass [53], Al_2O_3 $1.0 \times 10^8 \Omega\cdot\text{m}$ [38], and $\text{Fe}_2\text{O}_3 > 1.0 \times 10^{14} \Omega\cdot\text{m}$ at 333 K [53]. The values for the main components, CaCO_3 and SiO_2 , are significantly higher than that of graphite ($1.8 \times 10^{-5} \Omega\cdot\text{m}$ at 300 K) [40]. Thus, the current does not flow through the compressed RAP in the graphite mould. In the FEM simulation of the SPS process, the current flowed through the graphite mould instead of the compressed alumina powder [38,40]. Thus, the current flow profile of SPS using RAP was predicted as shown in Fig. 4. Moreover, the temperature distribution of alumina was nearly uniform, as confirmed by FEM simulation [40]. Thus, the temperature distribution in the compressed RAP during the SPS process was nearly uniform as well. Therefore, the HV distribution was nearly constant, and uniform densification of the sintered compacts took place.

Figure 5 shows the relationship between mechanical properties (flexural strength and modulus) and the sintering temperature. The flexural strength increased linearly from 30.4 to 74.2 MPa as sintering temperature increased from 1123 to 1223 K. Finally, a 78.9 MPa maximum flexural strength and an 81.4 GPa maximum flex-

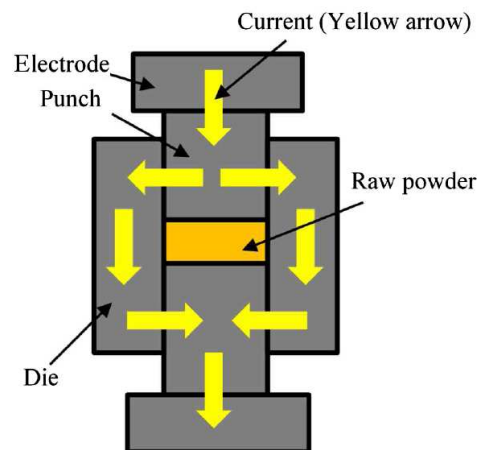


Figure 4. Current flow profile of SPS using RAP

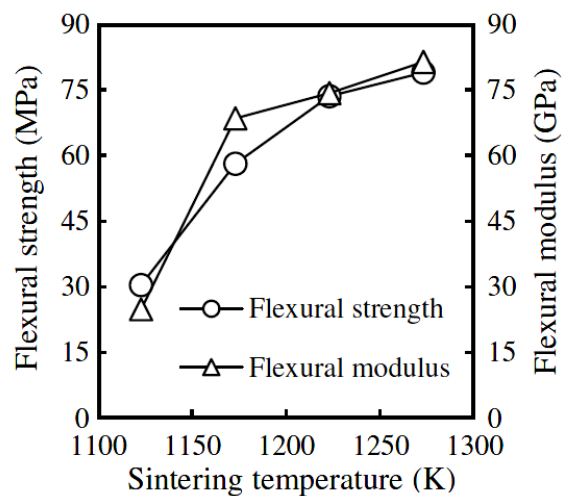


Figure 5. Relationship between mechanical properties and sintering temperature

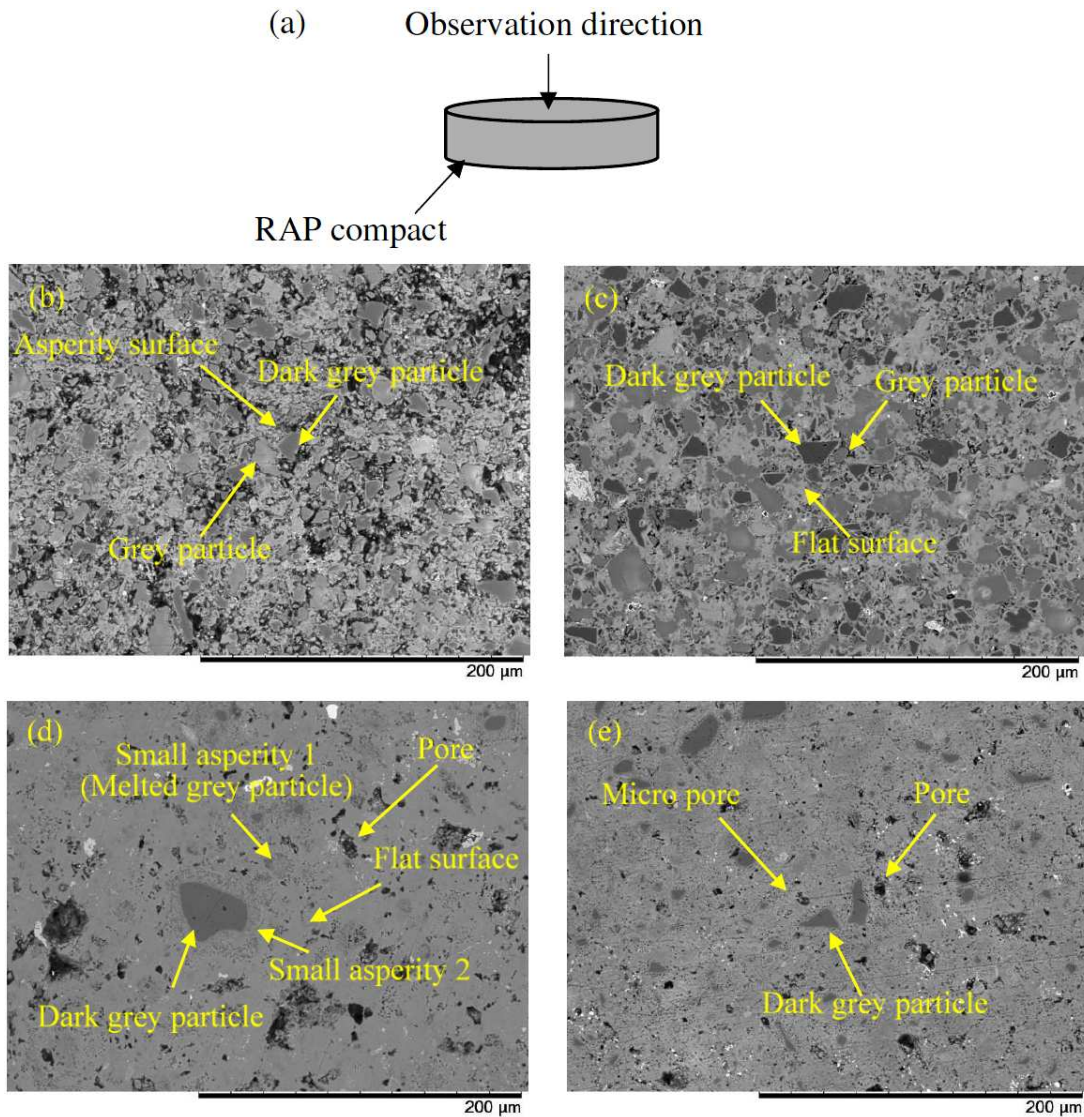


Figure 6. SEM images of the compact surface at each sintering temperature: a) observation direction, b) 1123 K, c) 1173 K, d) 1223 K and e) 1273 K

ural modulus were achieved at 1273 K. This value was significantly higher than that of ISO 13006 standards (35 MPa). The compressive strength of high-strength concrete is 118 MPa [54], whereas its flexural strength is generally one-seventh of the compressive strength. Thus, the flexural strength of high-strength concrete is 16.9 MPa. Additionally, the flexural strength of the fly ash SPS sintered compact is 75 MPa [32]. The flexural strength of glass ceramics, which are derived from industrial waste material, is 55–85 MPa, which is sufficient for the ceramics to be used as construction materials [42]. Therefore, at 1273 K, the SPS sintered compact exhibits satisfactory mechanical strength for use as construction materials.

To investigate the qualitative microstructure of the SPS sintered compacts, we observed the specimen surface using SEM. Figure 6 shows SEM images of the compact surface at each sintering temperature. These specimens were diamond polished in the final step; the

observation direction is shown in Fig. 6a. At 1123 K, the surface asperity of the compact is shown in Fig. 6b by an arrow. In addition, two types of colour particles were recognized, namely, dark grey and grey particles. As the sintering temperature increased to 1173 K (Fig. 6c), the surface flattened and contained dark grey and grey particles. Thus, solid-phase sintering progressed at 1173 K. Upon increasing the sintering temperature to 1223 K, as shown in Fig. 6d, a flat surface and some pores were visible. While the dark grey particles remained on the surface, the grey particles disappeared. Two types of small asperities were also recognized, as indicated by the arrows. Owing to the elliptical shape formed, the small asperities 1 are reasoned to be melted grey particles. The small asperities 2 are predicted to be the melted flat surface (Fig. 6c) because they are close to the dark grey particles. The SPS sintered compact, at 1223 K, can be considered a composite material with distributed dark grey particles in the grey matrix. Finally, at a 1273 K

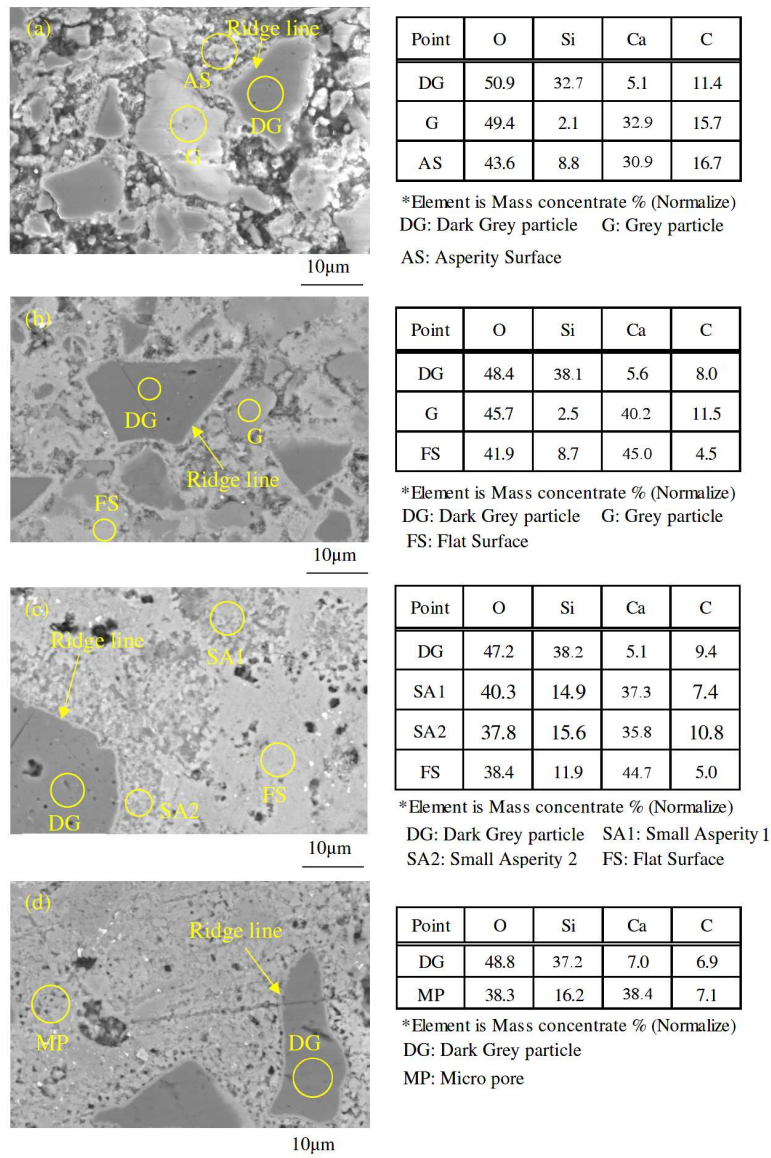


Figure 7. Element analyses of the compact surface using SEM-EDX at each sintering temperature: a) 1123 K, b) 1173 K, c) 1223 K and d) 1273 K

sintering temperature, the micropores were uniformly distributed on the surface containing the dark grey particles with few pores, as shown in Fig. 6e. These micropores were generated by the inner gas exiting from the melted grey matrix due to the high temperature of 1273 K. Thus, as seen in Fig. 2, the relative density at 1273 K decreased due to the generation of micropores.

To further evaluate the surface structure, we conducted an SEM-EDX analysis. Figure 7 shows the elemental analysis results for each sintering temperature. The dark grey particles (DG) mainly constituted oxygen and silicon at each measured sintered temperature. Moreover, the dark grey particles are evidence of the non-melting phenomenon because the ridge line maintains its edge. Thus, this section contains silica-rich sand in the waste mortar. The grey particles (G), asperity surface (AS), flat surface (FS), small asperities (SA1 and SA2), and micropores (MP) are mainly composed

of oxygen and calcium. Therefore, these parts are the waste cement and fine aggregates (including shells of sea creatures) with rich limestone. This shows that the small asperities 1 in Figs. 6d and 7c were created by melted grey particles. Thus, at sintering temperatures above 1223 K, the grey matrix was generated by melting the waste cement and fine aggregate with rich limestone. In addition, the liquid-phase sintering phenomena between the dark grey particles and grey matrix occurred over a sintering temperature of 1223 K.

To examine the liquid-phase sintering phenomena of the SPS process using RAP, we conducted a TG-DTA analysis. Figure 8 shows the TG-DTA curves. The curves between air and N₂ were similar showing that the liquid phase formation temperature of the SPS is similar to that of conventional furnaces. Here, Figs. 1 and 8b showing the recycled fine aggregates have a similarity with that from previous report [12]. Thus, the ther-

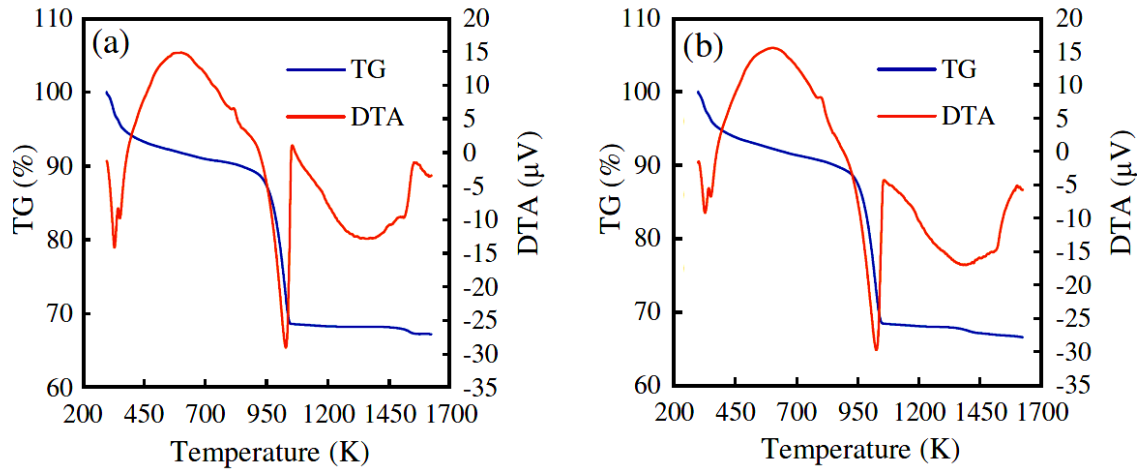
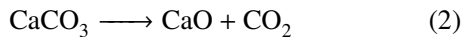


Figure 8. TG-DTA curves of RAP: a) in air and b) in N₂

mal characteristics of the aggregates shown in Fig. 8b have similarities to those in previous studies [12, 55]. The endothermic peak around 373 K is the vapour from the residual water present in the particles. Subsequently, dehydration occurs from the remaining Portlandite and a large endothermic peak is observed around 1023 K. The decrease in TG is due to the decarburization reaction of CaCO₃ and is expressed as follows:



Thus, limestone (CaCO₃) was converted to lime (CaO) at 1273 K. The endothermic peak around 1373 K and the slightly decreased TG show the RAP melting phenomenon. However, we observed melted RAP on the graphite mould at a sintering temperature of 1273 K (from Fig. 6e) after the experiment. We considered that the temperature difference between the compressed ceramics powder in the graphite mould and the die surface is nearly 373 K [38,40]. Thus, the compressed powder temperature rises to 1373 K at a sintering tempera-

ture of 1273 K. To further discuss the RAP melting phenomenon, we examined the densification behaviour of the SPS process. Figure 9 shows the relationship between displacement and temperature for each experiment. The displacement indicates the graphite punch position. The temperature was plotted over 873 K because it was measured using a radiation thermometer. The maximum displacement increased with increasing temperature until 1223 K; its values were 2.6 mm at 1123 K, 3.5 mm at 1173 K, 5.0 mm at 1223 K, and 4.9 mm at 1273 K. Therefore, the full densification temperature is considered at 1223 K. The compressed RAP temperature is predicted as 1323 K at 1223 K sintering temperature. The 1323 K RAP temperature approached the melting state, as shown in Fig. 8b. These results suggest that liquid phase formation occurred beyond a sintering temperature of 1223 K. To discuss the reinforcing behaviour of the compact sintered at 1273 K, we examined the element composition in Fig. 7d. As cited before, the dark grey particles are silica-rich sand whereas the grey matrix constitutes waste cement and limestone-rich fine aggregates. As shown in Eq. 2, the limestone was converted to lime at a sintering temperature of 1273 K. Hence, the grey matrix mainly constituted CaO. As mentioned, the HV of CaO ceramics is 190–260 and that of glass is 420. Thus, we predicted that the dark grey particle hardness is higher than that of the grey matrix. This indicates that the dark grey particles acted as reinforcement particles in the SPS sintered compact.

The SPS process model using RAP is shown in Fig. 10. Here, the sample constituents are mainly pores, silica-rich sand particles, and calcium-rich particles, which generated a grey matrix after sintering. It is assumed that the current does not flow into the compressed RAP, as shown in Fig. 4. Thus, the influence of current distribution on solid- and liquid-phase sintering is low. At a firing temperature ≤1223 K, the SPS process was mainly solid-phase sintering. Then, liquid-phase sintering progressed between the sand and melted calcium-rich particles at a sintering temperature

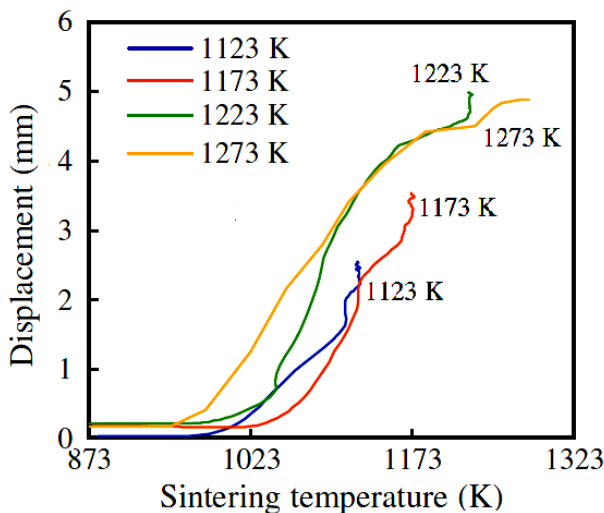


Figure 9. Relationship between displacement and temperature for each experiment

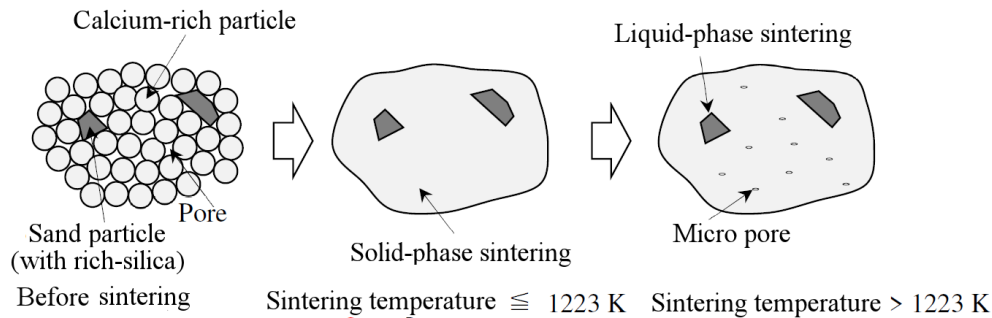


Figure 10. The SPS process model using RAP

>1223 K. The dark grey particles, which are considered to be sand particles, were enclosed by the melted grey matrix in Fig. 7c. Thus, improvement in wettability was expected between the sand particles and grey matrix at a sintering temperature over 1223 K due to the liquid-phase sintering phenomenon similar to that in the SPS process using fly ash and clay [32]. Furthermore, inner micropores were formed by inner gas due to the high sintering temperature. This phenomenon was predicted by the TG-DTA curves, which showed a melting temperature of 1373 K. Therefore, at the sintering temperature of 1273 K, the compact density decreases due to the formation of inner micropores at a high sintering temperature, as indicated by the arrows in Fig. 6e. However, the flexural strength and modulus showed maximum values at 1273 K due to improved wettability between the sand particles and grey matrix. These results indicate that the waste cement, which is the bottleneck for re-mixing concrete, played an effective role as a binder to reinforce sand particles.

In conclusion, RAP could be recycled as a ceramic raw material for construction materials due to a nearly 80 MPa flexural strength [30,42,46]. However, the mechanical properties of the SPS sintered compacts can be improved by further investigation of SPS processing conditions such as applied pressure and decreasing particle diameter. In addition, we used Okinawan concrete waste, which includes sea sand, limestone, and sea creature shells. For future studies, we will investigate the details of SPS processing conditions and the application of RAP made from ordinary concrete waste.

IV. Conclusions

To develop a novel method for recycling concrete waste, this study fabricated a ceramics using recycled aggregate powder (RAP) by applying the SPS method. In particular, the effect of sintering temperature on the mechanical properties of the RAP compact was investigated and the results are summarized as follows:

1. The maximum relative density was 1.0 (density value 2.8 g/cm^3) at a sintering temperature of 1223 K, but it decreased at 1273 K.
2. The density gradient was not recognized in the proposed sintered compact because the HV was almost

uniformly distributed. The maximum HV was 393 at a sintering temperature of 1273 K.

3. The flexural strength and modulus of the proposed sintered compact increased with sintering temperature. The maximum flexural strength and modulus were 78.9 MPa and 81.4 GPa, respectively, at a sintering temperature of 1273 K.
4. The sintered compact, beyond a sintering temperature of 1223 K, was composed of dark grey inclusions and a grey matrix-like composite material. SEM-EDX element analysis results showed that the dark grey inclusions were silica-rich sand particles in the waste mortar. The grey matrix was generated by melting the waste cement and fine limestone aggregate.
5. The TG-DTA curve of RAP and displacement on SPS processing showed the RAP melting phenomenon over 1223 K. Therefore, the mechanical properties, at a sintering temperature of 1273 K, were improved due to the enhanced wettability between the sand particle and the grey matrix by the progression of the liquid-phase sintering phenomenon.

Acknowledgements: This research work was partly supported by the Japan Society for the Promotion of Science KAKENHI (Project: Area number 19K05100). We would like to thank Machi Clean Co. Ltd for providing the waste concrete sample.

References

1. C. Meyer, "The greening of the concrete industry", *Cem. Concr. Composite.*, **31** (2009) 601–605.
2. V.W.Y Tam, M. Soomro, A.C.J. Evangelista, "A review of recycled aggregate in concrete applications (2000 - 2017)", *Const. Bldg. Mater.*, **172** (2018) 272–292.
3. B. Huang, X. Wang, H. Kua, Y. Geng, R. Bleischwitzet, "Construction and demolition waste management in China through the 3R principle", *Resour. Conser. Recyc.*, **129** (2018) 36–44.
4. T. Hongo, K. Igarashi, A. Iizuka, A. Yamasaki, "Preparation of high strength geopolymer hardened material from waste concrete", *Jpn. Resour. Processing.* (in Japanese), **59** (2012) 137–140.
5. C.S. Poon, D. Chan, "Feasible use of recycled concrete aggregates and crushed clay brick as unbound road sub-base", *Constr. Build. Mater.*, **20** (2006) 578–585.
6. I. Vegas, J.A. Ibáñez, J.T. San José, A. Urzelai, "Construc-

- tion demolition wastes, Waelz slag and MSWI bottom ash: a comparative technical analysis as material for road construction”, *Waste Manage.*, **28** (2008) 565–574.
7. I. Vegas, J.A. Ibañez, A. Lisbona, A. Sáez de Cortazar, M. Frías, “Pre-normative research on the use of mixed recycled aggregates in unbound road sections”, *Constr. Build. Mater.*, **25** (2011) 2674–2682.
 8. A. Barbudo, F. Agrela, J. Ayuso, J.R. Jiménez, C.S. Poon, “Statistical analysis of recycled aggregates derived from different sources for sub-base applications”, *Constr. Build. Mater.*, **28** (2012) 129–138.
 9. J.R. Jiménez, J. Ayuso, F. Agrela, M. Lopez, A.P. Galvín, “Utilisation of unbound recycled aggregates from selected CDW in unpaved rural roads”, *Resour. Conserv. Recy.*, **58** (2012) 88–97.
 10. J.R. Jiménez, J. Ayuso, A.P. Galvín, M. Lopez., F. Agrela, “Use of mixed recycled aggregates with a low embodied energy from non-selected CDW in unpaved rural roads”, *Constr. Build. Mater.*, **34** (2012) 34–43.
 11. L. Evangelista, J. de Brito, “Mechanical behavior of concrete made with fine recycled concrete aggregates”, *Cem. Concr. Composite.*, **29** (2007) 397–401.
 12. L. Evangelista, M. Guedes, J. de Brito, A. C. Ferro, M. F. Pereira, “Physical, chemical and mineralogical properties of fine recycled aggregates made from concrete waste”, *Constr. Build. Mater.*, **86** (2015) 178–188.
 13. A.M. Wagih, H.Z. El-Karmoty, M. Ebid, S.H. Okba, “Recycled construction, and demolition concrete waste as aggregate for structural concrete”, *HBRC Journal.*, **9** (2013) 193–200.
 14. A. Ajdukiewicz, A. Kliszczewicz “Influence of recycled aggregate on mechanical properties of HS/HPC”, *Cem. Concr. Compos.*, **24** (2002) 269–279.
 15. H. Shima, H. Tateyashiki, R. Matsushashi, Y. Yoshida, “An advanced concrete recycling technology and its applicability assessment through input-output analysis”, *J. Adv. Concr. Technol.*, **3** (2005) 53–67.
 16. S.W. Tabsh, A.S. Abdelfattah, “Influence of recycled concrete aggregates on strength properties of concrete”, *Constr. Build. Mater.*, **23** [2] (2009)1163–1167.
 17. M. Aineto, A. Acosta, I. Iglesias, “The role of a coal gasification fly ash as clay additive in building ceramic”, *J. Eur. Ceram. Soc.*, **26** (2006) 3783–3787.
 18. N. Chandra, P. Sharma, G.L. Pashkov, E.N. Voskresenskaya, S.S. Amritphale, N.S. Baghel, “Coal fly ash utilization: low temperature sintering of wall tiles”, *Waste Manage.*, **28** (2008) 1993–2002.
 19. A. Zimmer, C.P. Bergmann, “Fly ash of mineral coal as ceramic tiles raw material”, *Waste Manage.*, **27** (2007) 59–68.
 20. C. Li, Y. Zhou, Y. Tian, Y. Zhao, K. Wang, G. Li, Y. Ghai “Preparation and characterization of mullite whisker reinforced ceramics made from coal fly ash”, *Ceram. Int.*, **45** (2019) 5613–5616.
 21. F. Andreola, L. Barbieri, A. Corradi, I. Lancellotti, T. Manfredini, “Utilisation of municipal incinerator grate slag for manufacturing porcelainized stoneware tiles manufacturing”, *J. Eur. Ceram. Soc.*, **22** (2002) 1457–1462.
 22. L. Barbieri, A. Corradi, I. Lancellotti, T. Manfredini, “Use of municipal incinerator bottom ash as sintering promoter in industrial ceramics”, *Waste Manage.*, **22** (2002) 859–863.
 23. K. Dana, S.K. Das, “Partial substitution of feldspar by B.F. slag in triaxial porcelain: Phase and microstructural evolution”, *J. Eur. Ceram. Soc.*, **24** (2004) 3833–3839.
 24. Z.B. Ozturk, E.E. Gultekin, “Preparation of ceramic wall tiling derived from blast furnace slag”, *Ceram. Int.*, **42** (2015) 12020–12026.
 25. S. Ghosh, M. Das, S. Chakrabarti, S. Ghatak, “Development of ceramic tiles from common clay and blast furnace slag”, *Ceram. Int.*, **28** (2002) 393–400.
 26. E. Karamanova, G. Avdeev, A. Karamanov, “Ceramics from blast furnace slag, kaolin and quartz”, *J. Eur. Ceram. Soc.*, **31** (2011) 989–998.
 27. M.M. Jordán, M.B. Almendro-Candel, M. Romero, J.Ma. Rincón, “Application of sewage sludge in the manufacturing of ceramic tile bodies”, *Appl. Clay Sci.*, **30** (2005) 219–224.
 28. H. Shao-Hua, H. Shen-Chi, F. Yen-Pei, “Recycling technology - Artificial lightweight aggregates synthesized from sewage sludge and its ash at lowered co melting temperature”, *Environ. Prog. Sustainable Energy.*, **32** (2013) 740–748.
 29. S.R. Teixeira, A.E. de Souza, G.T. de Almeida Santos, A.F.V. Peña, Á.G. Miguel, “Sugarcane bagasse ash as a potential quartz replacement in red ceramic”, *J. Am. Ceram. Soc.*, **91** [6] (2008) 1883–1887.
 30. M.A.S. Schettino, J.N.F. Holanda, “Processing of porcelain stone ware tile using sugarcane bagasse ash waste”, *Process. Appl. Ceram.*, **9** (2015) 17–22.
 31. I. Fukumoto, E. Nakamura, Y. Kanda, “Fabrication of composite material using bagasse ash and carbonized bagasse by spark plasma sintering”, *Trans. Jpn. Soc. Mech. Eng. Ser A* (in Japanese), **78** [786] (2012) 201–212.
 32. I. Fukumoto, Y. Kanda, “Mechanical properties of composite material using coal ash and clay”, *J. Sol. Mech. Mater. Eng.*, **3** [5] (2009) 739–747.
 33. G. Kaneko, M. Mori, H. Kitagawa, K. Hasezaki, and H. Tanaka, “Preparation and characterization of sintered coal fly-ash bulk material by spark plasma sintering”, *J. Jpn. Soc. Powder. Metallurgy* (in Japanese), **53** (2006) 503–506.
 34. K. Hasezaki, A. Nakashita, G. Kaneko, H. Kakuda, “Unburned carbon behaviour in sintered coal fly-ash bulk material by spark plasma sintering”, *Mater. Trans.*, **48** [12] (2007) 3062–3065.
 35. E. Nakamura, I. Fukumoto, Y. Kanda, “Fabrication of composite materials using coal ash and aluminium sludge by spark plasma sintering”, *J. Solid. Mech. Mater. Eng.*, **5** (2011) 967–977.
 36. D.M. Hulbert, D. Jiang, D.V. Dudina, A.K. Mukherjee, “The synthesis and consolidation of hard materials by spark plasma sintering”, *Int. J. Refract. Met. Hard Mater.*, **27** (2009) 367–375.
 37. Z.A. Munir, U. Anselmi-Tamburini, M. Ohyanagi, “The effect of electric field and pressure on the synthesis and consolidation of materials: a review of the spark plasma sintering method”, *J. Mater. Sci.*, **41** (2006) 763–777.
 38. U. Anselmi-Tamburini, S. Gennari, J.E. Garay, Z.A. Munir, “Fundamental investigations on the spark plasma sintering/synthesis process: II. Modeling of current and temperature distributions”, *Mater. Sci. Eng. A*, **394** (2005) 139–148.
 39. E. Nsiah-Baafi, A. Andrews, “Fabrication of mullite from lithomargic clay via spark plasma sintering”, *Ceram. Int.*, **43** (2017) 14277–14280.

40. M. Sakkaki, F.S. Moghanlou, M. Vajdi, M.S. Asl, M. Mohammadi, M. Shokouhimehr, “Numerical simulation of heat transfer during spark plasma sintering of zirconium diboride”, *Ceram. Int.*, **46** (2020) 4998–5007.
41. F.J.H.T.V. Ramos, L.C. Mendes, S.P. Cestari, “Organically modified concrete waste with oleic acid”, *J. Therm. Anal. Calorim.*, **119** (2015) 1895–1904.
42. K. Ikeda, H. Kinoshita, R. Kawamura, K. Nagatomo, A. Yoshikawa, A. Hiratsuka, “Development of high strength glass-ceramics using industrial wastes”, *J. Jpn. Soc. Exp. Mech.* (in Japanese), **9** [3] (2009) 210–215.
43. K. Ikeda, H. Kinoshita, R. Kawamura, A. Yoshikawa, O. Kobori, A. Hiratsuka, “Production of high-strength glass-ceramics from industrial wastes using phase equilibrium diagram of CaO-Al₂O₃-SiO₂ system”, *J. Solid. Mech. Mater. Eng.*, **5** (2011) 209–218.
44. K. Ikeda, T. Tokumaru, H. Kinoshita, R. Kawamura, A. Yoshikawa, O. Kobori “Production glass and glass ceramics from industrial waste system by using phase equilibrium diagram of CaO-Al₂O₃-SiO₂ system”, *Trans. Jpn. Soc. Mech. Eng. Ser A* (in Japanese), **78** [789] (2012) 679–683.
45. T. Qingbo, W. Yue, X. Li’na, W. Xiuhui, G. Hong., “Preparation, and properties of glass-ceramics made from concrete sludge”, *R. Metal. Mater. Eng.* (in Chinese), **36** (2007) 979–982.
46. O.R. Njindam, D. Njoya, J.R. Mache, M. Mouafon, A. Messan, D. Njopwouo, “Effect of glass powder on the technological properties and microstructure of clay mixture for porcelain stoneware tiles manufacture”, *Constr. Build. Mater.*, **170** (2018) 512–519.
47. Y. Kanda, M. Abass, “Effective utilization of recycled fine aggregate powder as reinforcement particles in polyethylene composite”, *Polym. Polym. Compos.*, (2020) doi: 10.1177/0967391120951381.
48. Z. Wu, K.H. Khayat, C. Shi, “Effect of nano-SiO₂ particles and curing time on development of fiber-matrix bond properties and microstructure of ultra-high strength concrete”, *Cem. Concr. Res.*, **95** (2017) 247–256.
49. M. Wakamatsu, S. Shimizu, N. Takeushi, Y. Shioji, M. Tatemori, K. Onizuka, “Bending strength, and Weibull parameter of sintered lime fired at 1750 °C”, *Gypsum Lime* (in Japanese), **218** (1989) 18–23.
50. Z. Shen, M. Johnson, Z. Zhao, M. Nygren, “Spark plasma sintering of alumina”, *J. Am. Ceram. Soc.*, **85** (2002) 1921–1927.
51. I. Fukumoto, S. Mekaru, S. Shibata, K. Nakayama, “Fabrication of composite material using alumina agglomerated sludge and aluminum powder by spark plasma sintering”, *JSME Int. J. Series A*, **49** (2006) 91–94.
52. M. Nifuku, T. Higashi, S. Masuda, “A study on static electrification of coal and calcium carbonate powders during pneumatic transportation”, *J. Inst. Electrostat. Jpn.* (in Japanese), **11** (1987) 185–191.
53. W.D. Kingery, H.K. Bowen, D.R. Uhlmann, *Introduction to ceramics*, John Wiley & Sons, Inc, Second Ed., 1976.
54. S.Y.N. Chen, G.F. Peng, J.K.W. Chan, “Comparison between high strength concrete and normal strength concrete subjected to high temperature”, *Mater. Struct.*, **29** (1996), 616–619.
55. G. Villain, M. Thiery, G. Platret, “Measurement methods of carbonation profiles in concrete: Thermogravimetry, chemical analysis and gammadensimetry”, *Cem. Concr. Res.*, **37** (2007) 1182–1192.